

Supplementary Materials for

Acoustic Manipulation of Disk-in-Sphere Endoskeletal Droplets

Gazendra Shakya[†], Tao Yang[†], Yu Gao, Apresio K. Fajrial, Baowen Li, Massimo Ruzzene, Mark A. Borden and Xiaoyun Ding*

*Corresponding author. Email: xiaoyun.ding@colorado.edu

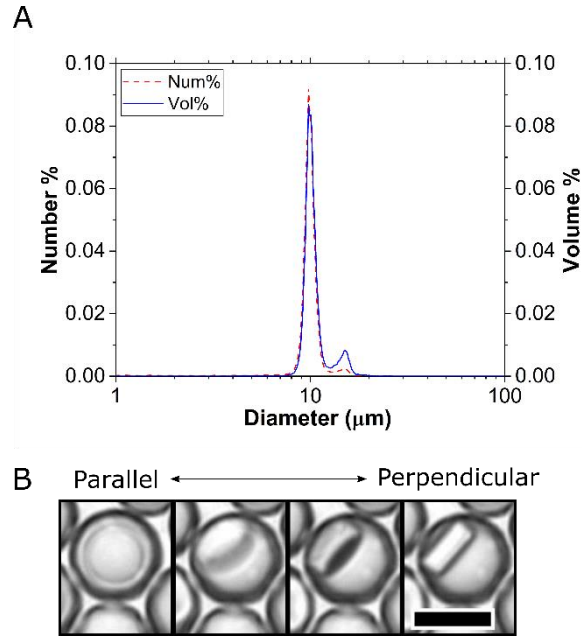
[†] These authors contributed equally to this work.

This PDF file includes:

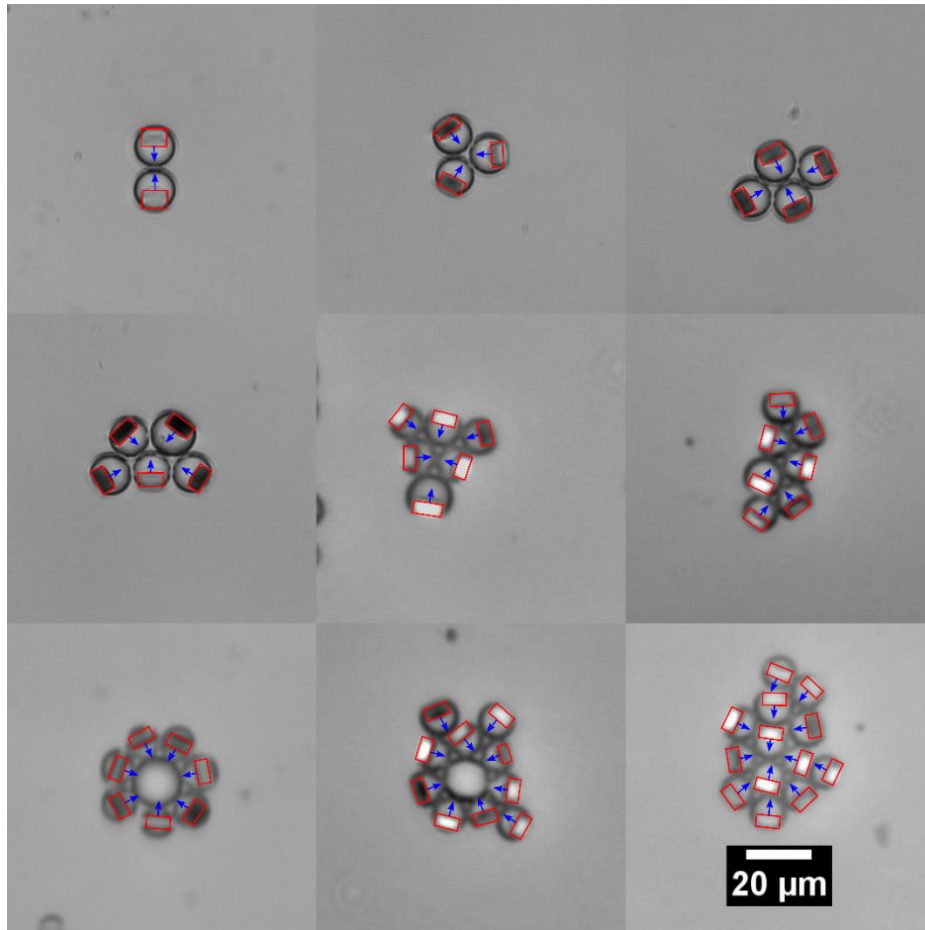
Supplementary Section 1 to 5
Supplementary Figures 1 to 10
Supplementary Table 1
Captions for Supplementary Movies 1 to 11
References

Other Supplementary Materials for this manuscript include the following:

Supplementary Movies 1 to 11



Supplementary Figure 1 : Endoskeletal Droplets. **A.** Size distribution of the endoskeletal droplets generated using microfluidics (shown in Fig. 1) showing both the number percent (red dashed line) and volume percent (blue solid line). **B.** Series of images showing the same endoskeletal droplet with rotating and translating disk from parallel orientation to perpendicular orientation. Scale bar: 10 μm .



Supplementary Figure 2: Clusters containing different numbers of endoskeletal droplets under SSAW. The disks are oriented in such a way that the normal (blue arrow) drawn from the basal plane of the disk (red rectangle) always points to the centroid of the cluster. This behavior is consistent irrespective of the number of droplets in the cluster.

Supplementary Section 1: Comparison of secondary radiation interactions between two polystyrene particles and PFH droplets

The secondary radiation interaction energy between two PFH droplets on the plane parallel to the wave propagation direction close to anti-nodal line (i.e. Eqn. 4 in the main text) can be obtained when $kh = \pi/2$ is substituted into Eqn. 19 in Silva and Bruus ¹:

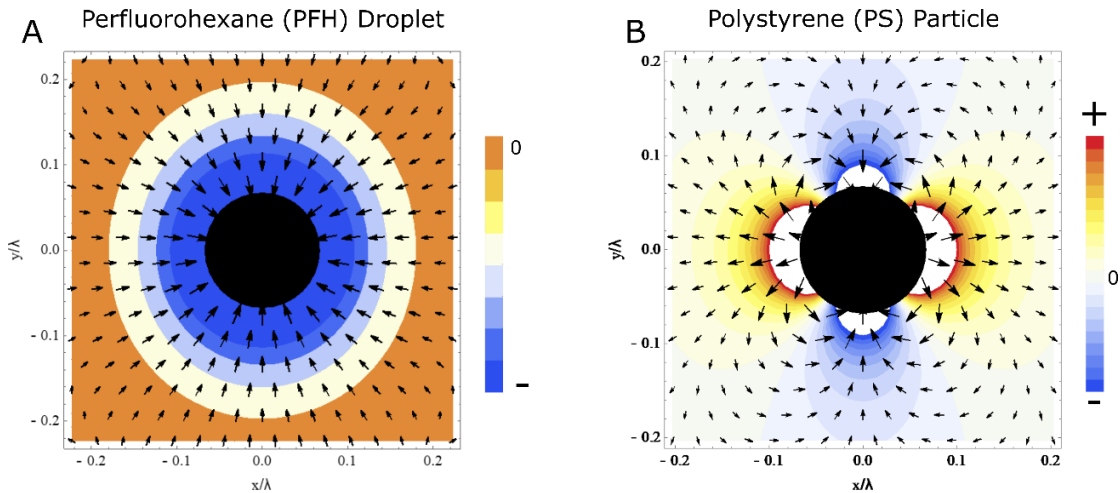
$$U_{sec} = \pi E_0 k^3 a^6 \left[\frac{2}{3} f_{1,l/w} f_{0,l/w} \sin(krcos\delta) \cos\delta \left(\frac{coskr}{(kr)^2} + \frac{sinkr}{kr} \right) - \frac{4}{9} \frac{f_{0,l/w}^2 \cos(krcos\delta) coskr/kr}{kr} \right] \quad (S1)$$

For $r \sim a$, i.e. in short range, $kr \ll 1$, the second term in Eqn. S1 can be neglected and Eqn. S1 can thus be further simplified to Eqn. 4 after small angle approximations and trigonometric function simplifications where:

$$\begin{aligned} \sin(krcos\delta) coskr &= \frac{1}{2} [\sin(krcos\delta + kr) + \sin(krcos\delta - kr)] \\ &\cong \frac{1}{2} [krcos\delta + kr + krcos\delta - kr] = krcos\delta \end{aligned} \quad (S2i)$$

$$\begin{aligned} \cos(krcos\delta) coskr &= \frac{1}{2} [\cos(krcos\delta + kr) + \cos(krcos\delta - kr)] \\ &\cong \frac{1}{2} \left[1 - \frac{1}{2}(krcos\delta + kr)^2 + 1 - \frac{1}{2}(krcos\delta - kr)^2 \right] \sim 1 \end{aligned} \quad (S2ii)$$

Similarly, when $kh = 0$ is substituted into Eqn. 19 in Silva and Bruus ¹, the secondary interaction between two PS particles can be obtained as:



Supplementary Figure 3: PFH vs PS patterning. The acoustic interaction pair potential U_{sec} (Eqn. 4) and U_{sec}' (Eqn. S3) (contours) and force $F_{sec} = -\nabla U_{sec}$ (or $F_{sec}' = -\nabla U_{sec}'$) (arrows) between two PFH droplets (A) and PS particles (B). Attraction in PS particles is anisotropic and angle dependent (attraction close to 90° , repulsion $\sim 0^\circ$) whereas attraction in PFH particles is isotropic (attracted from all angles). This results in the formation of clusters for PFH (as seen in Fig. 2H-J, 3C) whereas chains for PS (as seen in Fig. 3D).

$$U_{sec}' = \pi E_0 a^6 f_{1,p/w}^2 \frac{1+3 \cos 2\delta}{2r^3}, \quad (S3)$$

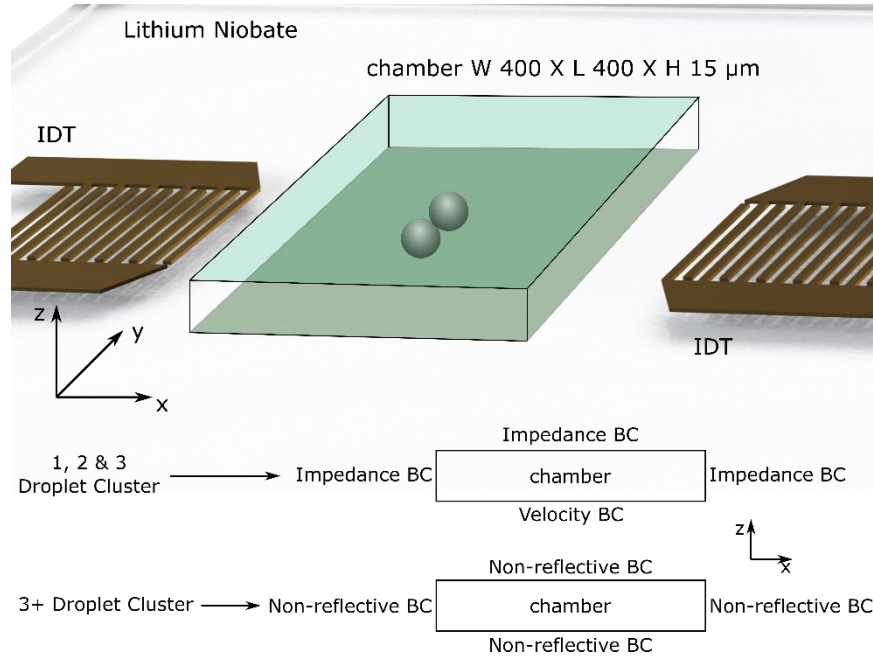
which is consistent with Eqn. 22a in Silva and Bruus¹ if $\delta = \pi/2$.

The acoustic interaction pair potential U_{sec} (Eqn. 4) and U_{sec}' (Eqn. S3) (contours in Supplementary Fig. 3) and force $F_{sec} = -\nabla U_{sec}$ (or $F_{sec}' = -\nabla U_{sec}'$) (arrows in Supplementary Fig. 3) between two PFH droplets and two polystyrene particles is thus compared in Supplementary Fig. 3. It is clearly seen for droplets with a negative acoustic contrast factor and a dominant monopole scattering factor, like PFH droplets, the interactions are almost isotropic and thus drive compact cluster formation (Fig. 3H-J, 3C). Conversely, for microparticles with a positive acoustic contrast factor (do not need a dominant dipole scattering factor) like polystyrene particles as the secondary interaction energy is dipolar and highly orientation dependent. The interaction from repulsive to attractive happens at so-called magic angle $\sim 54.7^\circ$ and the lowest energy occurs at $\delta = \pi/2$, resulting in chains as the most stable configurations under 1D standing wave (Fig. 3D). Shorter range and much weaker interactions can also be expected for two polystyrene particles compared to two PFH droplets.

Supplementary Section 2: Numerical simulation on skeletal disk orientations

Finite element simulations were performed using COMSOL (ver 5.0) to find the equilibrium disk orientations for endoskeletal droplet clusters. Here, the Helmholtz equations with endoskeletal droplet cluster configurations were solved numerically. Pressure domain acoustic *acpr* module in COMSOL was used to numerically solve the Helmholtz equation,

$$\nabla^2 \phi + k^2 \phi = 0 \quad (S4)$$



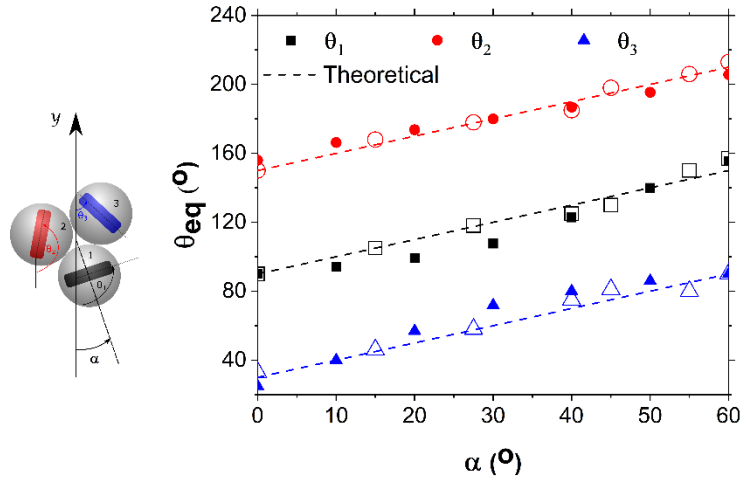
Supplementary Figure 4: COMSOL Schematic. Schematic of the finite element simulation performed in COMSOL showing the boundary conditions used for the simulations.

where ϕ is the particle velocity potential, i.e. $\mathbf{v}_1 = \nabla\phi$. The whole simulation domain is composed of W 400 μm ($\sim 2\lambda$, 20 MHz) $\times L$ 400 μm $\times H$ 18 μm ($\sim 3.6 a$) chamber (Supplementary Fig. 4) filled with water and PFH droplets and PFDD disks as separate *pressure acoustic (acpr)* domains. A 1D standing wave was implemented as the background field. Non-reflective boundaries were set for all the chamber surfaces following others²⁻⁴.

For small clusters like monomers and dimers, a velocity boundary condition following Devendra et, al.⁵ was applied to the bottom LiNbO₃ surface as the leaky wave was taken into consideration. All other surfaces bound by PDMS were taken as impedance boundaries implemented with PDMS acoustic properties due to computer memory constraints. Since the effect of the leaky wave is much less dramatic for clusters that are larger than trimers, only a background 1D standing wave was implemented along with perfectly matched layers for all the boundaries (Supplementary Fig. 4).

After solving the wave equations along with boundary conditions, the force and torque on an inner disk can be calculated via the integral of surface tensors along a surface enclosing the disk following Bruus⁶ as:

$$\begin{aligned} \mathbf{F} &= \iint \left(\left(\frac{\langle p_1^2 \rangle}{2\rho_l c_l^2} - \frac{\rho_l \langle \mathbf{v}_1 \cdot \mathbf{v}_1 \rangle}{2} \right) \hat{\mathbf{n}} + \rho_l \langle (\hat{\mathbf{n}} \cdot \mathbf{v}_1) \mathbf{v}_1 \rangle \right) ds \\ \boldsymbol{\tau} &= \iint \mathbf{r}_{so} \times \left(\left(\frac{\langle p_1^2 \rangle}{2\rho_l c_l^2} - \frac{\rho_l \langle \mathbf{v}_1 \cdot \mathbf{v}_1 \rangle}{2} \right) \hat{\mathbf{n}} + \rho_l \langle (\hat{\mathbf{n}} \cdot \mathbf{v}_1) \mathbf{v}_1 \rangle \right) ds \end{aligned} \quad (\text{S5})$$



Supplementary Figure 5: Disk angle vs cluster angle. Equilibrium angles (θ) for the i^{th} disk shown for various values for cluster orientation (α). The solid symbols show the calculated angles from the simulations (disk 1 - black square, disk 2 - red circle and disk 3 - blue triangle). The empty symbols show the experimental angles for the respective disks. The dotted line represents predictions based on cluster symmetry, i.e. $\theta_{i,eq} = \frac{5}{6}\pi - \frac{\pi}{3}i + \alpha$

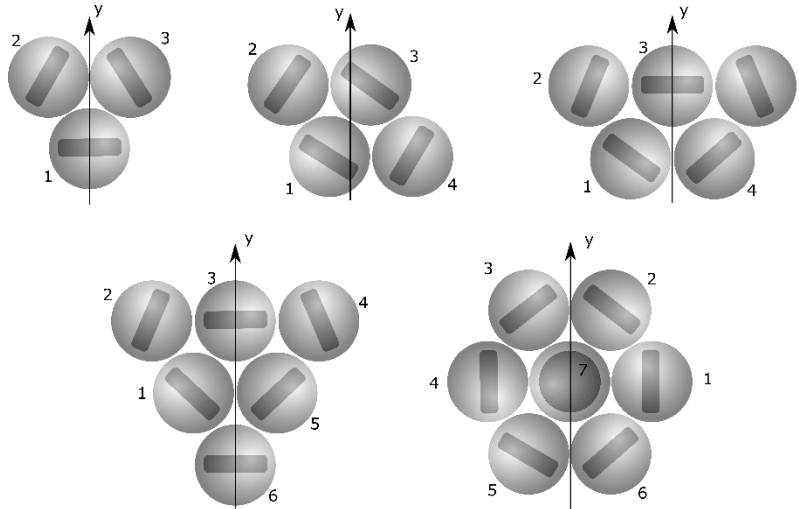
where \hat{n} is a unit normal vector pointing outwards the surface s , \mathbf{r}_{so} the position vector connecting the center of mass of disk/droplet and the point on the surface, p_1 and \mathbf{v}_1 is obtained from the solved wave equations.

As for the solid disk in a standing acoustic wave, the skeletal disk orientations are also determined by equilibrium zero torque configurations. The calculated torque from Eqn. S5 on i^{th} disk, $\tau_{z,i}$, inside a trimer droplet cluster was found $\tau_{z,i} \propto \sin(2(\theta_i - \alpha + \frac{\pi}{3}(i-1)))$ (Fig. 4A, 4B), where θ_i is the orientation angle of the disk in the i^{th} droplet and antinodal line (positive y axis) whereas α is defined as the angle between the antinodal line and the line joining the centroid and the center of the 1st droplet (which gives us the orientation of the whole cluster). Geometrically, the i^{th} disk equilibrium orientation should thus be $\theta_{i,eq} = \frac{5}{6}\pi - \frac{\pi}{3}i + \alpha$ (confirmed with changing α , Supplementary Fig. 5), i.e. the normal to each disk's basal plane points to the trimer centroid, which is consistent with experimental results (Supplementary Fig. 2, equilibrium θ values for different α shown in Supplementary Fig. 5).

Supplementary Table 1: Equilibrium angles (θ) of the disks in different cluster sizes calculated at $\alpha = 0$

# of Droplets	θ_1	θ_2	θ_3	θ_4	θ_5	θ_6	θ_7
3	90	155	24	-	-	-	-
4	65	167	65	167	-	-	-
5	51	162	90	130	18	-	-
6	57	160	90	20	123	90	-
7	0	58	122	0	58	122	NA

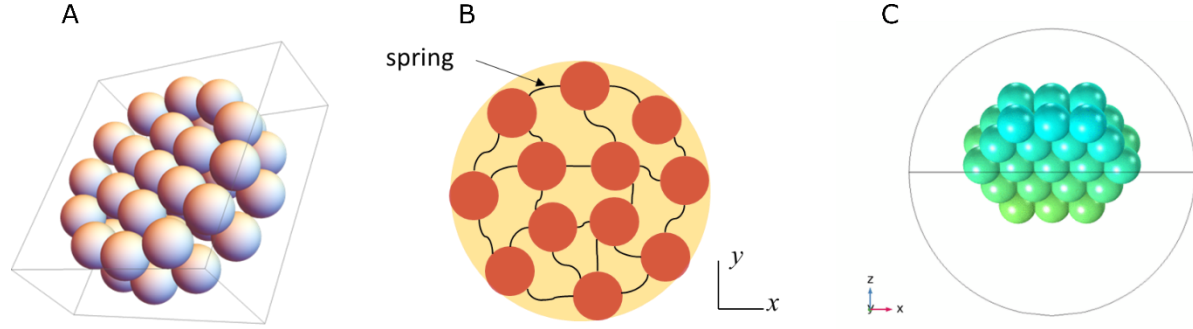
The same consistent simulation results were also confirmed for all other larger clusters. The equilibrium angles (calculated at $\alpha = 0$ from zero torque configurations) for cluster with 3 to 7 droplets are listed in the Supplementary Table 1 and their schematic is shown in Supplementary Fig. 6. These disk angles are consistent with the orientation of the disks seen in experiments (Fig. 2E-G, Supplementary Fig. 2) for clusters with same number of droplets.



Supplementary Figure 6: Droplet cluster schematic. Schematic of 3 to 7 droplet clusters showing i^{th} droplet. Disk orientations based on numerical simulation and the i^{th} disk angles are tabulated in Table S1. Compare with experimental disk orientations in Fig. 2E-G and Supplementary Fig. 4.

Supplementary Section 3: Dynamic Simulations

Note that torque calculations in Fig. 4A and Fig. 4B (also Supplementary Table 1, Supplementary Fig. 5 and Supplementary Fig. 6) assume that disks are at the droplet centers and non-moving. In experiments, because of its positive contrast factor with respect to the surrounding PFH environment, disks are pushed to the edges of the droplets (as seen in experimental results Fig. 2D-G, Supplementary Movie 1). Thus, disk dynamics simulations were also carried out. Each disk was represented by two-layer hexapolarly aligned ($N = 2 \times 19 = 38$) smaller spheres radius ($a_p = 1.34 \mu\text{m}$ with same disk density) with a rigid Hooken spring connected between two neighboring spheres (Supplementary Fig. 7).



Supplementary Figure 7: Schematic of the disk for dynamic simulations. **A.** Each disk is represented by two layered hexapolarly aligned smaller spheres. **B.** Each small sphere is connected with a rigid Hooken spring. **C.** Schematic of the constructed disk inside the droplet.

The external forces on each small sphere include pointwise radiation force $\mathbf{F}_{pri} = -\nabla U_{\text{rad}}$, which can be derived from Eqn.1 once the wave equation with fixed droplet position is solved, and the drag force $\mathbf{F}_{dp} = -6\pi\eta a_p \mathbf{v}_p$, where η is PFH liquid viscosity and \mathbf{v}_p is the small sphere instantaneous velocity. The inter-sphere Hooken spring force is given as: $\mathbf{F}_s = -k_s \sum_{i=1}^N (|\mathbf{r} - \mathbf{r}_i| - r_0) \frac{\mathbf{r} - \mathbf{r}_i}{|\mathbf{r} - \mathbf{r}_i|}$ and in order to confine spring forces only between neighboring spheres, a cutoff length $r_c = 2.8 a_0$ was applied. The instantaneous velocity on the i^{th} small sphere $\mathbf{v}_{p,i}$ can be solved via a set of ODE equations:

$$m_p \frac{d\mathbf{v}_{p,i}}{dt} = \mathbf{F}_{pri} + \mathbf{F}_{dp,i} + \mathbf{F}_{s,i} (r_{ij} < r_c) \quad (\text{S6})$$

where $m_p = \rho_s \frac{4}{3} \pi a_0^3$ is the mass of each small sphere. Thus, the whole disk trajectory and orientation at any moment can be obtained afterwards. As seen from the simulated disk dynamics inside a trimer cluster (Supplementary Movie 4), disks standing perpendicular to the substrate were pushed to the edge of the enclosing droplet with long axis parallel to the contact line, consistent with experimental results. The consistent orientations with equilibrium torque calculations also indicate symmetric field distributions along axes of symmetry of the cluster.

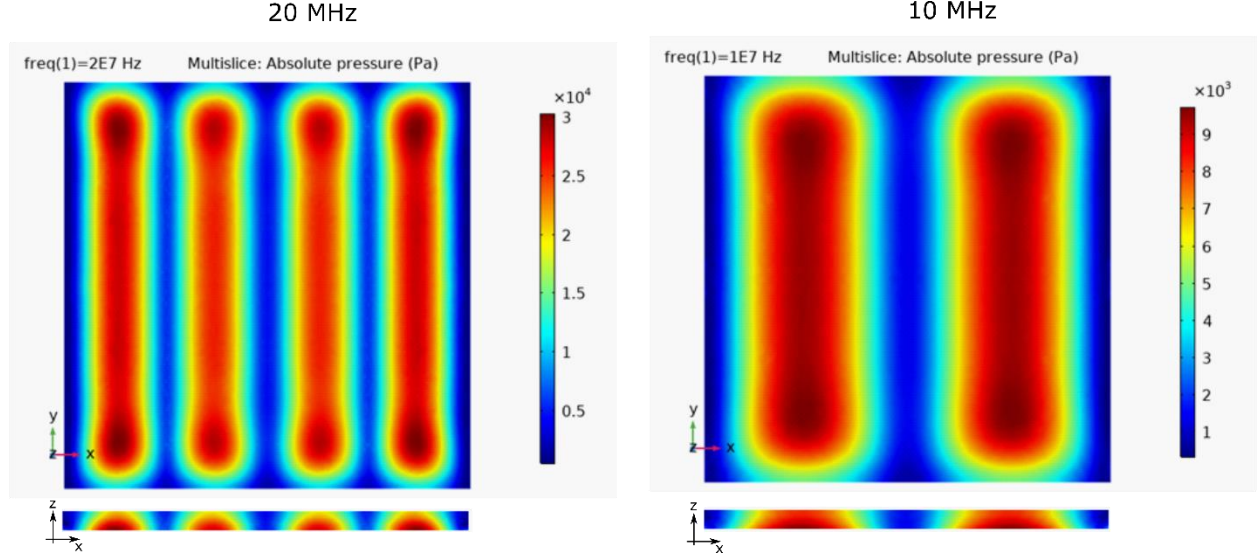
Supplementary Section 4: Contribution of Leaky Wave

For the real case, surface acoustic wave is more complicated when the leaky wave from lithium niobite substrate moving into fluid medium is taken into consideration. Following the numerical simulation process developed by Nama, et al.⁷, Devendra et al.⁵, and Barnkob, et al.⁸, a velocity boundary condition (Eqn. 12 in Ref.²) was set on the bottom PDMS surface, while acoustic impedance boundaries on all other surfaces (Supplementary Fig. 4). The calculated pressure distribution without droplets is shown in Supplementary Fig. 9. It's clearly seen that in addition to a standing wave in x axis, a sophisticated pressure distribution along z axis is observed. As in our case the channel height is confined at a height of $\sim 3a$, a quasi-standing wave without a fully developed period is observed as in Supplementary Fig. 8. Since particle velocity \mathbf{v}_1 inside droplets is the sum of primary or incident particle velocity \mathbf{v}_{pri} and particle velocity from scattering wave \mathbf{v}_{sec} and related with acoustic pressure as:

$$\mathbf{v}_1 = \mathbf{v}_{pri} + \mathbf{v}_{sec} = \frac{\nabla p_1}{i\rho_l c_l} = \frac{1}{i\rho_l c_l} (\nabla p_{pri} + \nabla p_{sec}) \quad (S7)$$

where p_{pri}/p_{sec} is the incoming/scattered acoustic pressure, i is the imaginary unit. As $\nabla p_{pri} = \nabla p_{in} = -p_0(\sin(k_{LN}x) \cos(k_w \sin \theta_R z) \hat{\mathbf{x}} + \cos(k_{LN}x) \sin(k_w \sin \theta_R z) \hat{\mathbf{z}})$ and incident particle velocity at droplet center can be approximated as $\mathbf{v}_{pri} = \frac{1}{i\rho_l c_l} \nabla p_{pri} = \frac{p_0}{i\rho_l c_l} \sin(k_w \sin \theta_R a) \hat{\mathbf{z}} \sim \frac{p_0}{i\rho_l c_l} k_w \sin \theta_R a \hat{\mathbf{z}}$, where $x = 0$ (antinodal line), $z = a$ and $k_w \sin \theta_R a \ll 1$.

As the monopole term is dominant over dipole term in our system, secondary scattering velocity



Supplementary Figure 8: Leaky wave pressure distributions. Pressure amplitude distributions on a chamber (400 X 400 X 15 μm) formed by 1D standing waves (acoustic waves moving in positive and negative x-axis). Fully formed standing waves are generated in the x-axis. Since the channel height is much smaller than the wavelength, quasi-standing waves are formed in the z axis. This is seen for both 20 MHz and 10 MHz wave.

potential $\phi_{sec} = \frac{p_{sec}}{i\rho_l c_l}$ can be simplified from Eqn. S6 in ⁴ as:

$$\phi_{sec} \sim \phi_{sec,0} = i\omega f_{0,l/w} \frac{a^3 p_{in}(\mathbf{r}_s) e^{ik_w r}}{3\rho_l c_l^2 r} = i f_{0,l/w} \frac{a^3 p_0 k_l e^{ik_w r}}{3\rho_l c_l r} \quad (\text{S8})$$

where $\mathbf{r}_s = (0,0, a)$ is the position vector of the scatterer and $p_{in}(\mathbf{r}_s) = p_0 \cos(k_w \sin \theta_R a) \sim p_0$. Thus secondary particle velocity \mathbf{v}_{sec} can be simplified as:

$$\mathbf{v}_{sec} = \nabla \phi_{sec} = -i f_{0,l/w} \frac{a^3 p_0 k_l}{3\rho_l c_l} \frac{1}{r^2} \hat{\mathbf{r}} \quad (\text{S9})$$

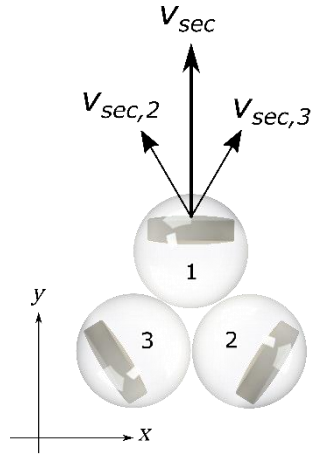
The secondary particle velocity therefore is purely radial and is along the y-axis in the case of dimer droplets.

For larger cluster like a trimer, if assuming the multibody scattering as the sum of binary scattering from neighborhooding droplets,

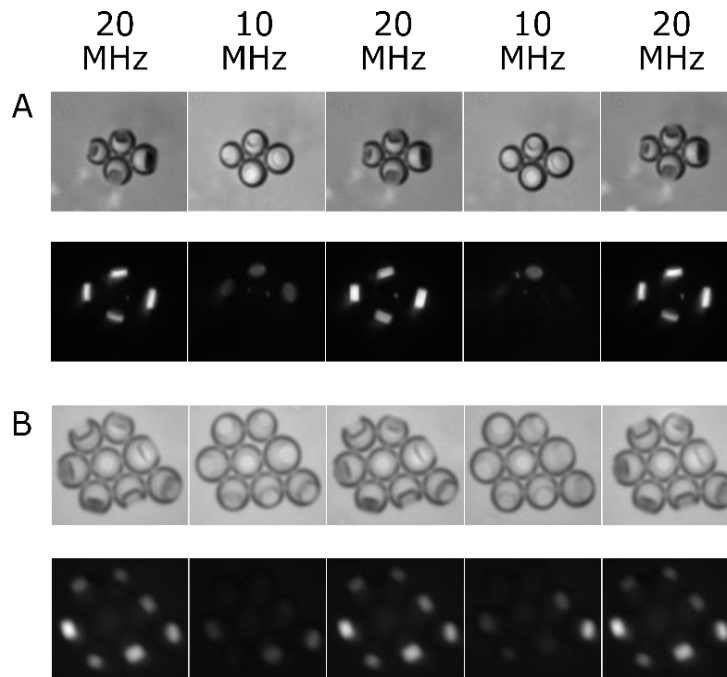
$$\mathbf{v}_1 = \mathbf{v}_{pri} + \sum \mathbf{v}_{sec,ij} \quad (\text{S10})$$

Since from Eqn. S9, the secondary scattering velocity \mathbf{v}_{sec} is along the radial direction, the sum of all secondary scattering from neighboring droplets on any droplet thus is along the line connecting droplet centroid to the whole cluster centroid (see Supplementary Fig. 9 for schematics for a trimer

cluster). More importantly, the amplitude of summed secondary scattering velocity becomes larger as: $|\mathbf{v}'_{sec}| = \sqrt{3}|\mathbf{v}_{sec}|$. So total particle velocity aligns with x axis with an angle $\text{atan}(1/3) \sim 18.4^\circ$ and disk will align more steeper with xy plane compared with a dimer cluster.



Supplementary Figure 9: Sum of secondary scattering velocity. Schematic of a cluster with three droplets showing the effects of secondary radiation force on disk 1 from droplet 2 and 3.



Supplementary Figure 10: External control of disk orientation. Series of images showing the corresponding switching between a perpendicular to a parallel orientation of the disks along with changing frequencies from 20 to 10 MHz and vice versa for a 4 droplet cluster (**A**) and a 8 droplet cluster (**B**) (Movie S11 for corresponding video). Top figures show brightfield images whereas bottom figures show CPM images.

Supplementary Section 5: Supplementary Movie Captions

Supplementary Movie 1: Video showing disk interactions when standing SAW is turned on. Note that when standing SAW is turned on, the solid disks start orienting when it comes close to other droplets. Also note the change in orientation of the disks as the size of the droplet cluster changes.

Supplementary Movie 2: For a single droplet, when the SAW is turned on, the solid disk flips up to the top and orients parallel to the substrate (parallel to xy plane).

Supplementary Movie 3: For a cluster with two droplets, The droplets first form the cluster when the SAW is turned on and then the disks orient such that they are they are midway between the parallel and perpendicular orientations ($\sim 45^\circ$ from the xy plane).

Supplementary Movie 4: Dynamic simulations of cluster containing 3 droplets at 20 MHz shows the disks being pushed to the edges of the cluster as seen in experiments (Fig. 2E). Left shows the xy view and right shows the xz view.

Supplementary Movie 5: Dynamic simulation of a single droplet. Because of the primary radiation force (and the absence of secondary radiation force from neighboring droplets) from the traveling wave in z axis, the disks float up to the top and are parallel to the surface (xy plane). Left shows the xy view and right shows the xz view.

Supplementary Movie 6: Dynamic simulation of a 2 droplet cluster at 10 MHz (top) and 20 MHz (bottom). Here, left column is the xy view and the right column is the yz view. Since the secondary radiation force is more sensitive to frequency, decreasing frequency would decrease the effect of the secondary radiation force. Hence, the disks are more parallel to the surface for 10 MHz than for 20 MHz.

Supplementary Movie 7: Video showing disk orientation when 10 MHz standing SAW is turned on. Note that the disks orient parallel to the surface (as opposed to perpendicular for 20 MHz in Supplementary Movie 1).

Supplementary Movie 8: Dynamic Simulations of a 3-droplet cluster showing the disk orientations at 10 MHz (top) and 20 MHz (bottom). The left column is the xy view and the right column is the xz view.

Supplementary Movie 9: The orientation of the disk can be tuned by changing the frequencies. The video shows a 3-droplet cluster where the frequency of the acoustic waves are switched back and forth between 10 and 20 MHz.

Supplementary Movie 10: Same as Supplementary Movie 9 but using CPM instead of brightfield. Under CPM, disks in perpendicular orientation (@20 MHz) are clearly seen whereas disks in parallel orientation (@10 MHz) are not seen.

Supplementary Movie 11: Similar to Supplementary Movies 9 and 10 for 4 droplet cluster and 8 droplet cluster.

References

1. Silva, G. T. & Bruus, H. Acoustic interaction forces between small particles in an ideal fluid. *Physical Review E* **90**, (2014).
2. Glynne-Jones, P., Mishra, P. P., Boltryk, R. J. & Hill, M. Efficient finite element modeling of radiation forces on elastic particles of arbitrary size and geometry. *The Journal of the Acoustical Society of America* **133**, 1885–1893 (2013).
3. Garbin, A. *et al.* Acoustophoresis of disk-shaped microparticles: A numerical and experimental study of acoustic radiation forces and torques. *The Journal of the Acoustical Society of America* **138**, 2759–2769 (2015).
4. Simon, Andrade, Desmulliez, Riehle, & Bernassau. Numerical Determination of the Secondary Acoustic Radiation Force on a Small Sphere in a Plane Standing Wave Field. *Micromachines* **10**, 431 (2019).
5. Devendran, C., Albrecht, T., Brenker, J., Alan, T. & Neild, A. The importance of travelling wave components in standing surface acoustic wave (SSAW) systems. *Lab on a Chip* **16**, 3756–3766 (2016).
6. Bruus, H. Acoustofluidics 7: The acoustic radiation force on small particles. *Lab on a Chip* **12**, 1014 (2012).
7. Nama, N. *et al.* Numerical study of acoustophoretic motion of particles in a PDMS microchannel driven by surface acoustic waves. *Lab on a Chip* **15**, 2700–2709 (2015).
8. Barnkob, R. *et al.* Acoustically Driven Fluid and Particle Motion in Confined and Leaky Systems. *Physical Review Applied* **9**, (2018).